IIETA International Information and Engineering Technology Association
Advancing the World of Information and Engineering

Annales de Chimie - Science des Matériaux
Vol. 48, No. 6, December, 2024, pp. 887-898
Journal homepage: http://iieta.org/journals/acsm

Microstructural Evolution of NiTi-Coated Austenitic Stainless Steel Using TIG Cladding: Influence of Current Values

Abdul Sameea J. Jilabi*, Huda Th. Abuhameed

Faculty of Materials Engineering, University of Babylon, Hillah 51002, Iraq

Corresponding Author Email: sameeakilabi@gmail.com

https://doi.org/10.18280/acsm.480614

Received: 21 October 2024
Revised: 12 December 2024
Accepted: 23 December 2024
Available online: 31 December 2024

Keywords:
dendritic solidification, TIG cladding, NiTi coatings, 316 austenitic stainless steel

ABSTRACT

Nowadays, surface modification of austenitic stainless steels has become a necessity for the scientific and industrial communities. Cladding made of tungsten inert gas (TIG) is one efficient way to modify the surfaces of these steels. The study aims to probe the influence of TIG cladding current intensities (80-160A), and thus heat energy input on microstructures of NiTi coatings deposited on AISI-316 austenitic stainless steel. 1 mm diameter pre-placed NiTi wires with a cladding travel speed of 87 mm/min. were used to deposit a distinct clad layer-substrate interfacial bonding in all the coated samples. Scanning electron and optical microscopies revealed different microstructures throughout the clad layers, mostly NiTi-based solid solution dendrites with minor phase precipitates distributed through the matrix. The energy dispersive spectroscopy proved that the amounts of chromium and iron elements diluted from the substrate into the molten NiTi layer increase (53.9 wt.% and 13.7 wt.% respectively) with increasing cladding current intensity at the expense of Ni and Ti contents. The diluted elements can lead to the formation of a B2 (NiTiFeCr) dendritic structure during solidification. X-ray diffraction testing revealed the presence of different phases and compounds forming the coating layers mainly NiTi solid solution, γ(Fe,Ni), $Cr_{0.19}Fe_{0.7}Ni_{0.11}$ and $Cr_{1.36}Fe_{0.52}$.

1. INTRODUCTION

Stainless steels are important alloys because of their special and demanding qualities. Their significance is demonstrated by the range of uses they have, from straightforward ones like furniture and kitchenware to highly intricate ones like spacecraft and construction applications. The three main microstructure types of stainless steels are ferritic, austenitic and martensitic. These three main microstructures can be used to categorize stainless steels into a number of major classes. Precipitation hardening, duplex, martensitic, ferritic, and austenitic stainless steels are among them [1, 2]. Their mechanical, chemical and physical characteristics differ according to their chemical compositions. However, austenitic stainless steels are characterized by their ability to produce a self-protective oxide layer and resist corrosion, as well as by having a higher chromium content that improves resistance to oxidation and corrosion [3].

Austenitic stainless steels contain a minimum of 16% chromium and 6% nickel. 18/8 is the most often used austenitic stainless steel that contains 18% Cr and 8% Ni. Additional elements such as molybdenum, titanium, and/or copper can be added to modify or enhance their properties, making them suitable for many critical heat and corrosion resistance applications [4]. However, there are also many industrial components work continuously in severe conditions such as high temperatures and stresses, cyclic forces, high pressure and impacts, which can result in components wear and damage. In order to improve the efficiency and increase service life, surface modification of austenitic stainless steels has recently become necessary for the scientific community because the surface properties of wettability, adhesion, hardness, corrosion and wear resistance of new materials are frequently inadequate. Furthermore, it is difficult to find an alloy with a different surface behavior than the bulk for various reasons. In order to improve properties in metals and alloys to be suitable for severe environments, strategies of surface modification depend on a direct action on the metal/alloy or incorporating coatings provide these properties or functionalize its surface for complex requirements have to be applied [5].

NiTi (also named as Nitinol) is an intermetallic compound consists of Ni and Ti in almost equal ratio. It has been used in numerous non-medical and medical applications [6-8]. This broad range of uses may be due to one or more of NiTi's unique characteristics, including its shape memory effect, super elasticity, high fatigue strength, high damping capacity, high corrosion resistance and strong biocompatibility [9]. In addition to having corrosion resistance similar to that of austenitic stainless steels, NiTi has been shown to have very good cavitation erosion resistance [9-13]. When utilized in bulk, NiTi alloys are expensive materials that are difficult to machine [14]. For certain component material applications, surface enhancement is essential for improving surface material qualities and lowering costs. Because no new component parts need to be made, the cladding process has the

advantage of lowering production costs. Additionally, because cladding layers are rarely thicker than a few micrometers, less material is needed to create coating layers on large quantities of substrate materials, overcoming the material shortage [9]. Cladding improves a number of qualities, such as increased surface hardness and resistance to corrosion and wear. Due to their lower wear resistance, stainless steel materials are not utilized in high-wear components. Modifying the surface properties of stainless steel material components could be the answer to the aforementioned issue. Researchers investigating NiTi cladding on various grades of austenitic stainless steels using tungsten inter gas (TIG) and laser cladding have reported a number of works [15-18].

The TIG coating procedure builds up or adds a new layer to the substrate surface is commonly used to improve a substrate's surface qualities, including hardness and wear resistance. Other popular coating techniques, such electron beam coating and laser coating, alter the surface characteristics by simultaneously melting the coating and substrate. However, the usage of laser cladding is limited by the varied rate at which the laser beam is absorbed by various coatings, and the complicated parts created by laser cladding are costly and require sophisticated machinery. Fortunately, compared with other cladding processes, TIG cladding offers reduced equipment and maintenance costs, lower dilution ratio, greater deposition rate and ease of use. It is also suitable for a wide range of materials, easy to transport and widely available. In addition, both manual and automated operations can be employed [19]. Figure 1 shows the TIG cladding's primary function [20].

To the best of the author's knowledge, the only work that has employed the TIG approach to deposit NiTi clad layers on AISI 316 austenitic stainless steel substrates is Cheng et al.'s 2003 study [21], but manually using a 2 mm diameter NiTi filler wire. The deposit was mainly composed of a NiTi-based alloy with Fe and Cr in solid solution, together with some second phase particles.

In 2021, Kumar et al. [18] applied a 1 mm diameter NiTi wire coating to super austenitic stainless steel (904L) using the TIG cladding process. The feeding of NiTi filler wire was done manually to achieve a few mm deposition thickness. The effect of TIG current on the microstructure and phases formation of the clad surface were investigated. The EDS and XRD study of the NiTi coating layer confirmed the formation of NiTi, NiTi2 and B2 (NiTiFeCr) as major constituent phases in addition to some intermetallic (Cr-Fe-Ni).

The study aims to explore the effect of using various TIG cladding current intensities (80-160A), and thus heat energy input on the microstructures of NiTi coatings automatically deposited on AISI-316 austenitic stainless steel using 1 mm pre-placed NiTi wires.

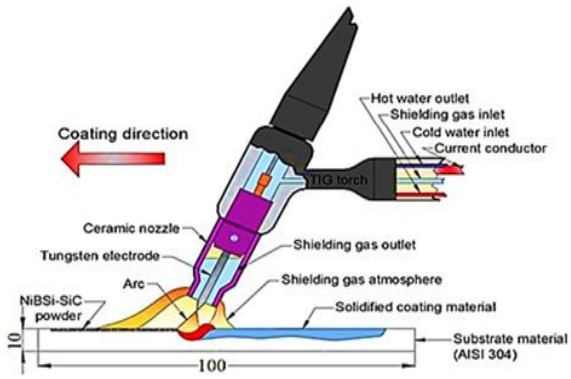

Figure 1. TIG cladding's primary function [21]

2. SPECIFICATIONS OF THE MATERIALS

Austenitic stainless steel AISI 316 plates of 10 × 70 mm were used in this experiment. Table 1 displays the chemical composition of the austenitic stainless steel plates that were utilized as substrates in this investigation in accordance with The American Institute of Iron and Steel (AISI) [22]. The components (substrates) that would be coated were made from the raw material, each piece had a length of 100 mm. The Spectro Max Metal Analyzer instrument was used to analyze the raw material's chemical composition. The chemical composition of the raw material utilized as a substrate is shown in Table 1 (averaged across three readings); it complies with the nominal AISI.

Table 1. The substrate material's chemical makeup, both nominal and actual

Alloy		Chemical Composition (wt.%)								Spec. Symbol (AISI)
		C	Mn	Si	Cr	Ni	Mo	P	S	
A.S.S.	Nominal (Maximum or Range)	0.08	2.0	0.75	16-18	10-14	2-3	0.045	0.03	316
	Actual	0.044	1.5	0.474	17.23	10.09	2.28	0.0143	0.0005	

2.1 Cladding materials

Materials used are AISI 316 stainless steel plates, 1 mm diameter NiTi (55,45) wire, polyvinyl alcohol (PVA).

2.2 Material for binding

PVA, or polyvinyl alcohol, was utilized as a binder to temporarily bind NiTi wires to the substrates surfaces. Table 2 shows the specifications of PVA.

2.3 Steps taken prior to the cladding procedure

Prior to the cladding procedure began, the following steps were accurately completed:

1. Grinding the surfaces of the substrates being coated by the use of a surface grinding machine to obtain the required roughness value.
2. Eliminating oils, grease, as well as other contaminants from the substrates' surfaces. The substrates were then ultrasonically washed with acetone and ethanol before being dried in warm air.
3. A magnetic stirrer was used to dissolve 4% PVA in 96% hot distilled water (50°C) for 15 minutes in order to create the binder. To maintain the NiTi wires under Ar gas flow during TIG cladding, the NiTi wires were bonded to the substrates surfaces using a binder of 4% PVA solution to create pre-placed NiTi wires to be subsequently deposited on the substrate (Figure 2).
4. Drying the components by an electric oven at 100℃ for 30 minutes.

Table 2. Specifications for polyvinyl alcohol

Product	PVA Code	Molecular Formula	Viscosity
MESE	8-88	$(C_4H_6O_2.C_2H_4O)x$	In a 4% aqueous solution, 8 mPa.s

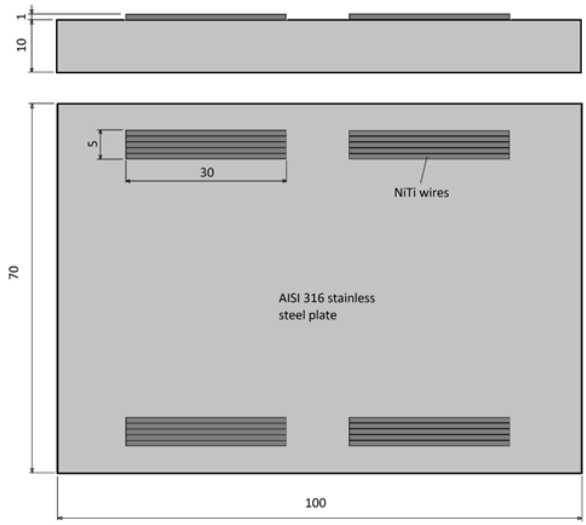

Figure 2. NiTi wires bonded to the surface of the AISI 316 stainless steel substrate

2.4 Tungsten inert gas cladding of NiTi wire coating on a substrate made of austenitic stainless steel

In order to move the tungsten arc over the clad layers at automatic and consistent rates, A TIG welding equipment and a lathe machine were used to complete the cladding procedure. For every coating layer, the substrate was where the arc igniting and extinguishing occurred (Figure 3). Table 3 displays the TIG cladding parameters derived from former research [23] and the trial-and-error approach.

After cladding, specimens were cut from the resulting samples (Figure 3b) with dimensions of 10 × 10 × 10 mm using Wire-EDM for micrography and XRD tests.

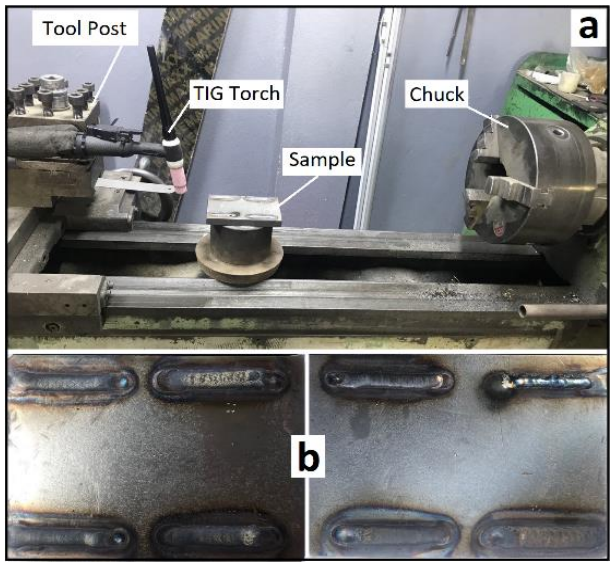

Figure 3. (a): a lathe machine with a TIG torch, (b): samples prior to test specimen preparation

Table 3. TIG cladding parameters of 316 stainless steel substrates

Cladding by the Use of 1 mm dia. Preplaced NiTi Wire					
Current Value (A)	80	100	120	140	160
Travel speed (mm/min.)	87				
Voltage (V)	15				
Position	Flat				
Polarity	DCEN				
Thickness of layer (mm)	1				
Flow rate of Ar gas (l/min)	10				
Purity of Ar gas (%)	99.999				
Length of arc (mm)	3				
Tungsten electrode dia.(mm)	2.4				
Type of tungsten electrode	Tungsten Thoriated ESAB-WT20				

3. RESULTS AND DISCUSSION

With the aid of the EDS, microanalysis of NiTi coatings deposited on 316 stainless steel substrates have been assessed by the OM and SEM. The phases and compounds made up the coating layers were also verified using the XRD test.

3.1 Macroscopic metallography

Understanding the AISI 316 austenitic stainless steel substrate material's microstructure is essential before talking about the microstructural differences among the coated samples. OM and SEM reveal in Figure 4 that the substrate alloy's microstructure consisted of austenite grains with twinning. As austenite stabilizers, the high concentrations of Ni (up to almost 10 weight percent) and Mn (up to 1.5 weight percent) in this steel's chemical composition are displayed in Table 1. This explains the appearance of austenite grains under the microscope [24]. Twinning in AISI 316 austenitic stainless steel is primarily affected by stacking fault energy (SFE) and crystallographic orientation, in addition to some other parameters such as strain rate, temperature and grain size. SFE is generally considered the most significant factor. 316 stainless steel has a relatively low SFE. This characteristic promotes twinning because it requires less energy to form a twin compared to materials with higher SFE. The orientation of the crystal lattice can also influence twinning, with certain orientations being more favorable for twin formation [25, 26].

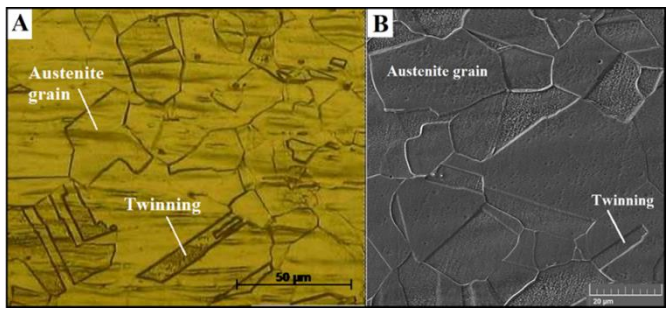

Figure 4. The substrate material's microstructure utilizing an OM (A) and SEM (B)

Under high strain rate conditions, twinning becomes more prevalent as a deformation mechanism. This is because twinning can occur more rapidly than dislocation slip at high strain rates. Twinning is however more likely to occur under

complex stress states, such as those encountered in forming processes. Lower temperatures make twinning a more favorable deformation mode, where the mobility of dislocations reduces. Moreover, smaller grain sizes can promote twinning, as there are more grain boundaries where twins can nucleate [25].

Each sample's microscopy revealed differences in the clad layer's and the substrate's surrounding areas' microstructures. These changes are explained by the wide thermal gradients that the sample is subjected to temperatures that range from the melting point to the substrate's temperature that is unaffected by heat, as well as the variations in the chemical composition of the coating layers. Usually, a fast rate of cooling follows, mostly due to the environment and the comparatively cold substrate.

Figure 5 demonstrates microstructures of the C1 sample coated with NiTi using the TIG cladding process at a travel speed of 87 mm/min and a current of 80 A. Three zones at different depths were micro-graphed along the cross sectional centerline of the clad layer.

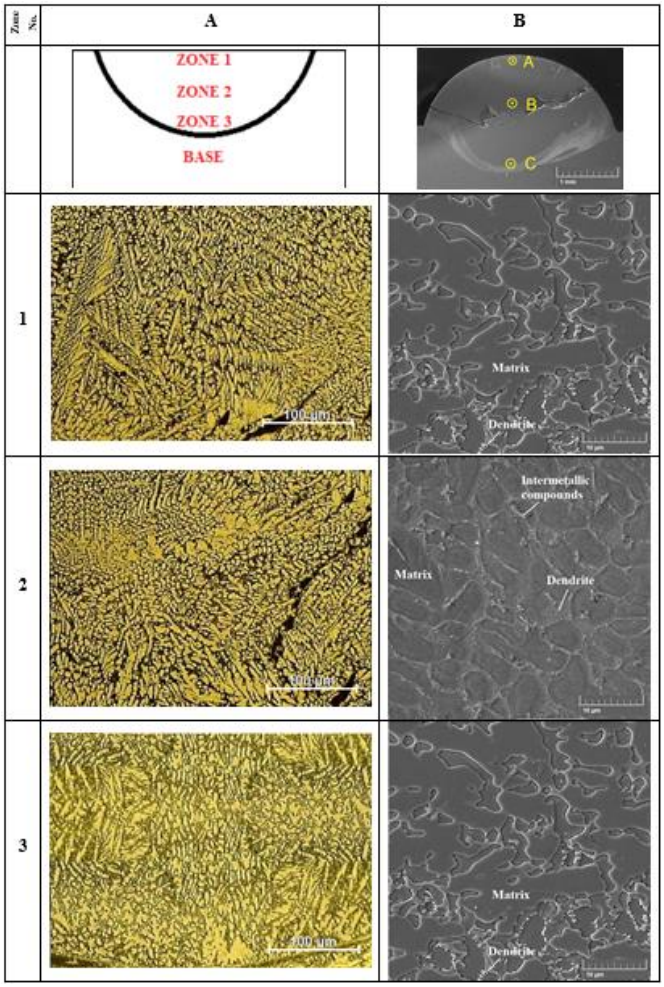

Figure 5. The C1 sample's microstructural map created using (A) OM and (B) SEM at different depths along the clad layer cross section's centerline

Figure 5 exhibits that the scanning electron and optical microstructures of Zone 1 (which is close to the coating surface) consist mainly of NiTi-based solid solution dendrites with minor phase precipitates (micrometers or less) distributed through the matrix. Figure 6 shows this zone's microstructure at greater magnifications.

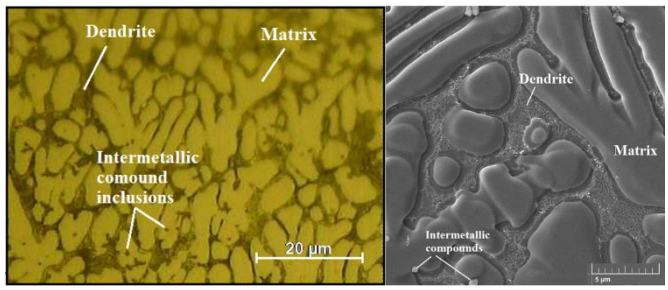

Figure 6. Microstructures of Zone 1 of C1 sample at greater magnifications

During the TIG cladding process, elements like chromium and iron from the AISI 316 stainless steel substrate can diffuse into the molten NiTi layer. Depending on their solubility in the NiTi solid solution, these elements might lead to the formation of a B2 (NiTiFeCr) dendritic structure during solidification. This is in line with the findings of Cheng et al. [21].

The matrix surrounding the NiTi-based dendrites is essentially a NiTi solid solution, similar in composition to the dendrites themselves. NiTi is the main material being deposited during cladding process. Although some intermixing with the stainless steel substrate occurs, the nickel and titanium from the NiTi feedstock material will remain key elements in the solidified layer. Most elements diluted from the stainless steel substrate have limited solubility in NiTi at high temperatures [27]. This means that they will not readily dissolve throughout the molten NiTi pool. Therefore, the matrix will essentially be a continuation of the NiTi solid solution that forms the dendrites, with possible traces of elements like chromium and iron based mainly on the specific diffusion and reaction rates. This is in agreement with that reported in 2005 by Chiu et al. [16]. There might be slight variations in the exact composition of the NiTi solid solution matrix compared to the dendrites. This could be due to factors like segregation and diffusion gradients.

During solidification of the clad layer molten pool, some elements might have a tendency to segregate towards the dendrite boundaries, slightly altering the local composition in the matrix. In addition, inter diffusion with the stainless steel substrate might not be completely uniform, leading to minor variations in the concentration of elements like chromium and iron within the matrix. These elements might react with Ni and Ti to form insoluble intermetallic compounds like NiCr or FeTi as minor phase precipitates at the dendrite boundaries or distributed through the matrix (SEM in Figure 5 and Figure 6). This is consistent with what Ozel et al. [28] revealed in 2008. These intermetallic compounds can also act as nucleation sites for the solidification of the NiTi-based dendrites. The presence of these solid intermetallic compounds within the molten NiTi pool lowers the activation energy required for NiTi crystal growth, promoting the formation of dendrites around them [29].

Microscopic examination revealed in Figures 5, 7 and 8 that Zones 2 and 3 have a similar microstructure to Zone 1, consisting of a mixture of equiaxed and columnar grains. However, it appears from observation of the microstructure of Zone 3 (Figures 5 and 8) that the dendrite content was greater. This could be attributed to the fact that the dilution effect in this zone is greater, as it is closer to the substrate. This leads to an increased possibility to form insoluble intermetallic compounds, which can serve as nucleation sites for dendrites, as mentioned above. Another reason is that because it is closer

to the cooling surface, the clad layer's bottom cools more quickly. Figure 9 exhibits the presence of an increased amount of intermetallic compounds at the interface between the clad layer and the substrate. This could be due to the greater Dilution's effect on the substrate material at this region. Such dilution was sufficient to obtain a good bonding with the substrate, which can be easily introduced by the TIG cladding technique [30]. It is clear from the figure that the grains of the clad layer in the region adjacent to the interface were a mixture of equated and columnar as well. The optical and scanning electron microscopy shows in Figure 9 that the austenitic grains of the substrate in the region close to the interface experienced substantial recrystallization, due to the heat generated during TIG cladding process.

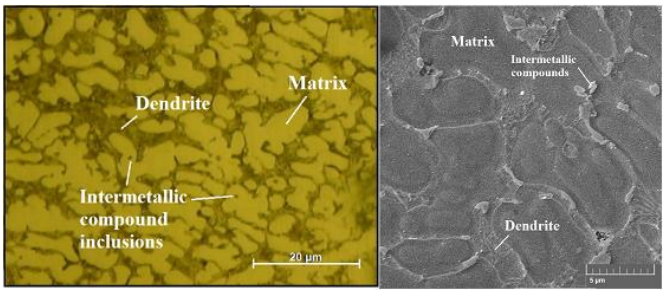

Figure 7. Microstructures of Zone 2 of C1 sample at greater magnifications

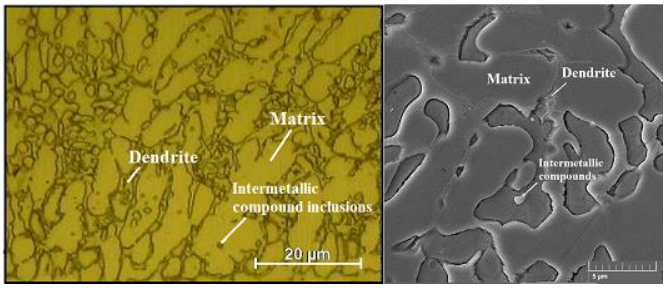

Figure 8. Microstructures of Zone 3 of C1 sample at greater magnifications

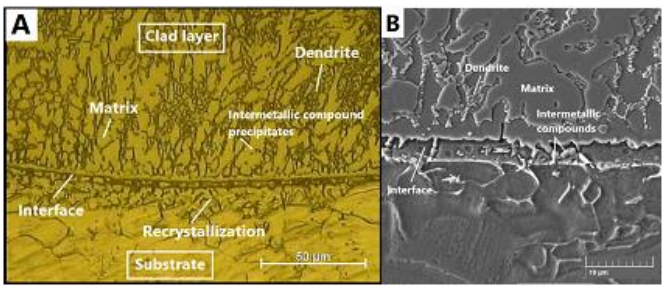

Figure 9. The microstructure of the C1 interface utilizing an OM (A) and SEM (B)

Energy-dispersive spectroscopy was conducted for the substrate material made of AISI 316 stainless steel, for zones A, B and C indicated in Figure 5, and along the C1 clad layer's cross sectional centerline. Table 4 shows the EDS examination of elemental composition for the substrate material, where it is clear that the substrate material's chemical composition is very similar to the nominal and actual composition that appeared in Table 1. Therefore, the EDS analysis can be considered a very good means for validation of the chemical composition of materials.

Table 4. EDS chemical composition analysis for AISI 316 steel substrate material

Chemical Composition (wt.%)				
Mn	**Si**	**Cr**	**Ni**	**Mo**
1.6	0.61	17.25	10.01	3.22

Table 5 and Figure 10 show the EDS elemental composition for the referred three different zones, and along the C1 cross section's centerline respectively.

Table 5. The C1 sample's elemental composition analyzed using EDS at different depths along the clad layer cross section's centerline

Element	Zone 1 [wt.%]	Zone 2 [wt.%]	Zone 3 [wt.%]
Ni	34.87	36.84	23.40
Ti	27.66	28.57	18.44
Cr	7.72	7.15	11.68
Fe	29.75	27.44	43.29

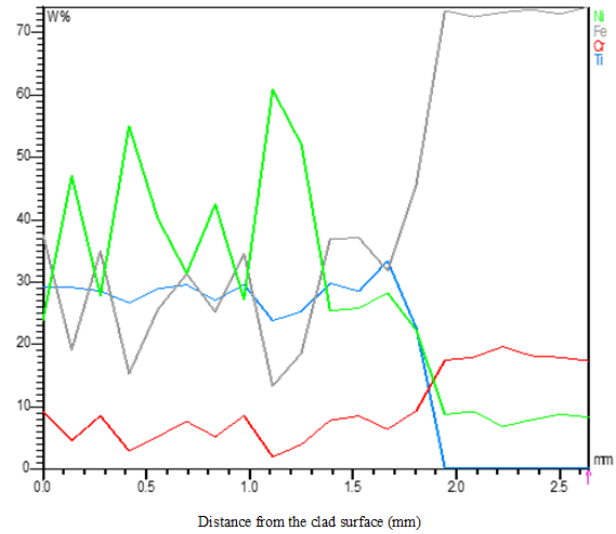

Figure 10. The EDS elemental composition along the C1 cross section's centerline

It is evident from Table 5 that there are significant contents of iron and chromium elements at the three test points (33.5 wt.% and 8.9 wt.% on average respectively), even though the preplaced NiTi wire consists of 55 wt.% Ni and 45 wt.% Ti, and is free of Fe and Cr. This is owing to the influence of dilution with the substrate material (AISI 316 austenitic stainless steel). The average nickel and titanium element contents across the clad layer are 31.7 wt.% and 24.9 wt.% respectively, with a ratio similar to that of NiTi feedstock wire (55:45).

It is also worth noting that the proportions of Fe and Cr elements in Zone 3, compared to those in Zones 1 and 2, are markedly higher at the expense of Ni and Ti contents. This is due to the fact that this zone is closer to the substrate, and therefore more dilution occurs. However, the chemical composition of Zones 1 and 2 is comparable.

Figure 10 shows fluctuations in weight percentages of the elements composing the clad layer while advancing along a line from the coating surface towards the substrate. This could be attributed to fact that this line passes through microstructures with different compositions as a result of segregation that takes place during solidification, including dendrites, intermetallic compounds and matrices.

XRD testing, which was conducted on the coating surface revealed the presence of different phases and compounds forming the coating layer. The analysis of the XRD graph with the help of analytical cards showed in Figure 11 that the main constituents of the C1 clad layer are NiTi solid solution, γ(Fe,Ni) and $Cr_{0.19}Fe_{0.7}Ni_{0.11}$ compound. This is in agreement with what was revealed in previous works [18, 28, 31]. A structure very similar to $Cr_{0.19}Fe_{0.7}Ni_{0.11}$ intermetallic compound (Cr_2Fe_7Ni), present as minor phase precipitates at the dendrite boundaries, was detected by XRD examination carried out in 2008 by Ozel et al. [28]. Another study achieved in 2020 by Shi et al. [31] revealed using XRD test the presence of a NiTi-based solid solution as a major phase and γ(Fe,Ni). This NiTi-based solid solution, along with Cr_2Fe_7Ni intermetallic compound was also detected in the XRD examination conducted in 2021 by Kumar et al. [18].

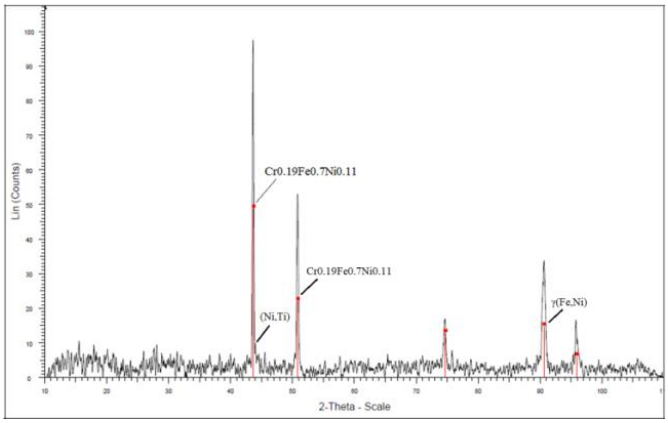

Figure 11. XRD graph of the surface of the C1 clad layer

3.2 The effect of cladding current value

Microscopic examination of the C2 sample produced by increasing the TIG cladding current value to 100 A with the travel speed of 87 mm/min. revealed in Figure 12 that the microstructure is noticeably finer. This could be attributed to the fact that increasing the cladding current value definitely increases the dilution with the substrate, which in turn increases the content of elements (diluted from the substrate) that form intermetallic compounds, which can serve as nucleation sites for dendrites. For the same reason, dendrite proportions across all three zones appear to be greater than that in the C1 sample's corresponding zones, as shown in Figures 13, 14 and 15. It can also be observed from Figures 12 and 15 that the dendrite content in the microstructure of Zone 3 is greater. This is because the dilution effect in this zone is greater due to its vicinity to the substrate, which can lead to an increased opportunity to form intermetallic compounds, and thus nucleation sites for dendrites. Figure 16 reveals that these intermetallic compounds at the interface of this sample are also greater than those appeared in the C1 sample.

In comparison with the C1 sample, the EDS chemical examination of composition at the three test points of the C2 sample exhibits in Table 6 that the average content of iron and chromium elements is significantly higher (42.3 wt.% and 10.6 wt.% respectively) at the expense of average nickel and titanium element contents (26.4 wt.% and 19.7 wt.% respectively). This proves that the dilution with the substrate in this sample was greater.

The proportions of Fe and Cr elements in Zone 3, compared to those in Zones 1 and 2, are also noticeably higher at the expense of Ni and Ti contents, because this zone is close to the substrate, and thus more dilution takes place.

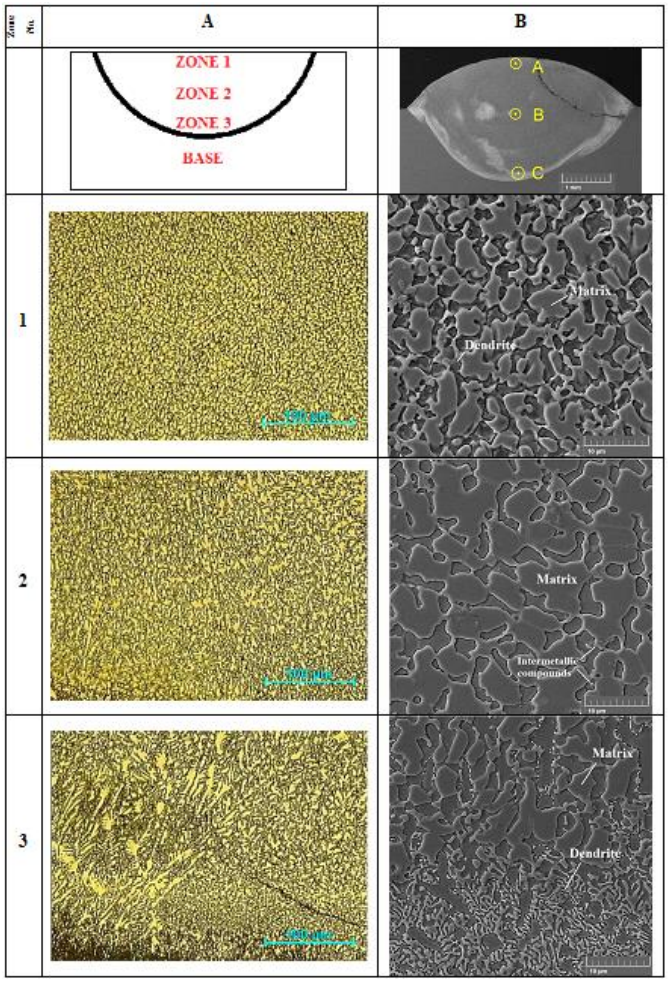

Figure 12. The C2 sample's microstructural map created using (A) OM and (B) SEM at different depths along the clad layer cross section's centerline

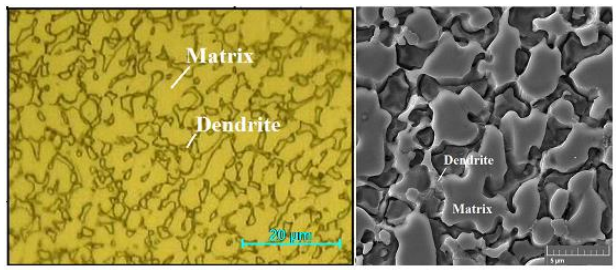

Figure 13. Microstructures of Zone 1 of C2 sample at greater magnifications

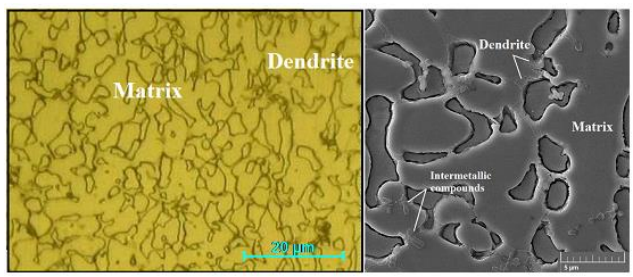

Figure 14. Microstructures of Zone 2 of C2 sample at greater magnifications

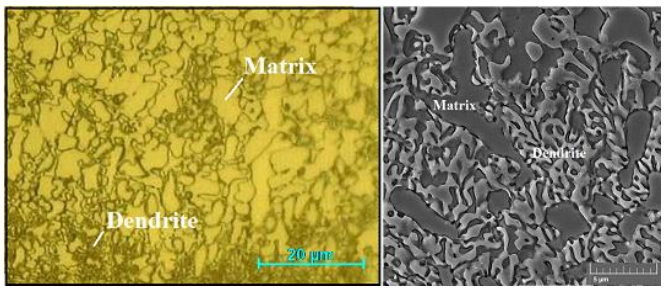

Figure 15. Microstructures of Zone 3 of C2 sample at greater magnifications

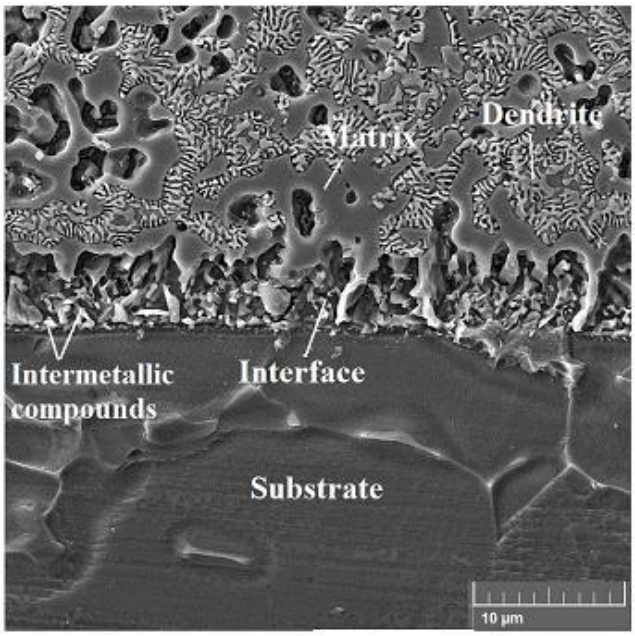

Figure 16. Scanning electron microstructure of the C2 interface

Table 6. The C2 sample's elemental composition analyzed using EDS at different depths along the clad layer cross section's centerline

Element	Zone 1 [wt.%]	Zone 2 [wt.%]	Zone 3 [wt.%]
Ni	27.38	27.84	23.95
Ti	21.27	21.08	16.87
Cr	10.20	10.07	11.58
Fe	41.14	41.01	44.59

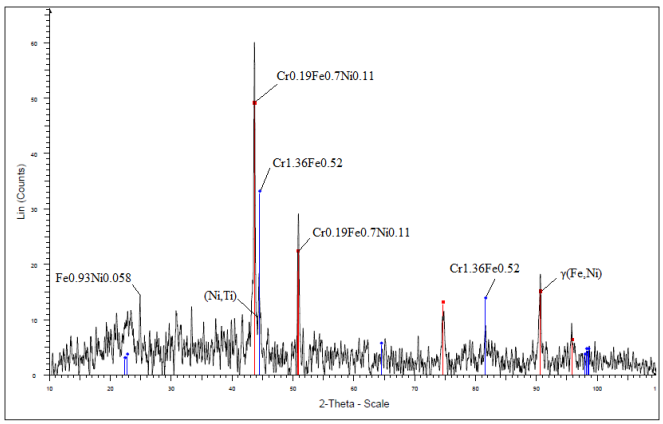

Figure 17. XRD graph of the surface of the C2 clad layer

XRD examination of the C2 surface revealed in Figure 17 that the main constituents of this clad layer are NiTi solid solution and γ(Fe,Ni), in addition to $Cr_{0.19}Fe_{0.7}Ni_{0.11}$, $Cr_{1.36}Fe_{0.52}$ and $Fe_{0.93}Ni_{0.058}$ compounds. Increasing the fraction of compounds present compared to those revealed in the XRD test of the C1 sample could be due to the increased dilution with the substrate as a result of using a higher cladding current value.

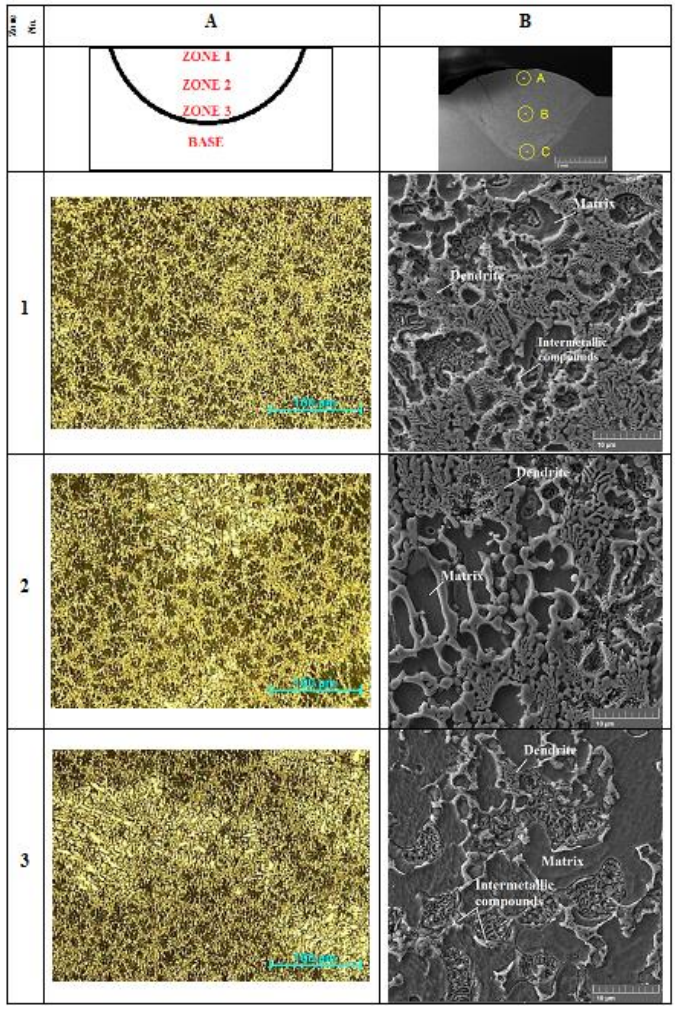

Figure 18. The C3 sample's microstructural map created using (A) OM and (B) SEM at different depths along the clad layer cross section's centerline

Microscopy of the C3 sample resulting from raising the TIG cladding current value to 120 A showed in Figure 18 a significant increase in the dendritic content at the matrix's expense in the microstructure of this sample at the three test points. This is because increasing the cladding current value increases the elements diluted from the substrate that form intermetallic compounds, which can serve as nucleation sites for dendrites. Another reason is that the increased cladding current value certainly increases the amount of heat energy input, reducing the cooling rate, which in turn gives the dendrite enough time to grow at the expense of the matrix [28, 32]. Figures 19-21 show the microstructure of the three zones through the cross section of this clad layer at greater magnifications. As expected, the amount of intermetallic compounds at the interface (Figure 22) and Zone 3 of the clad layer (closer to the interface) was greater than that in Zones 1

and 2. This is because the dilution influence is more as a result of the vicinity to the substrate.

The EDS chemical analysis of composition at the three test points of the C3 sample demonstrates in Table 7 that the average content of iron and chromium elements, compared to the C2 sample, is substantially higher (49.6 wt.% and 11.7 wt.% respectively) at the expense of average nickel and titanium element contents (22 wt.% and 16.7 wt.% respectively). This is because the dilution with the substrate in this sample was greater.

The Fe and Cr content elements in Zone 3, compared to those in Zones 1 and 2, are also noticeably higher at the expense of Ni and Ti contents, due to the proximity of this zone to the substrate, and thus more dilution occurs.

Table 7. The C3 sample's elemental composition analyzed using EDS at different depths along the clad layer cross section's centerline

Element	Zone 1 [wt.%]	Zone 2 [wt.%]	Zone 3 [wt.%]
Ni	22.67	21.74	21.71
Ti	16.95	18.97	14.22
Cr	11.56	10.88	12.50
Fe	48.82	48.41	51.57

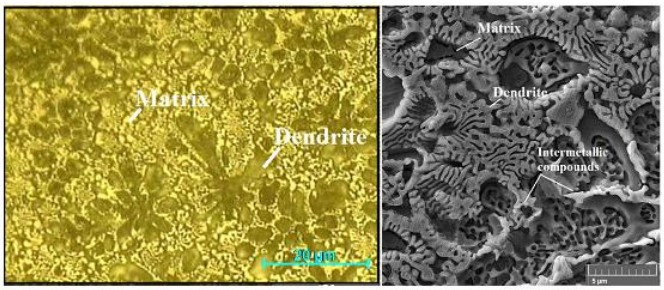

Figure 19. Microstructures of Zone 1 of C3 sample at greater magnifications

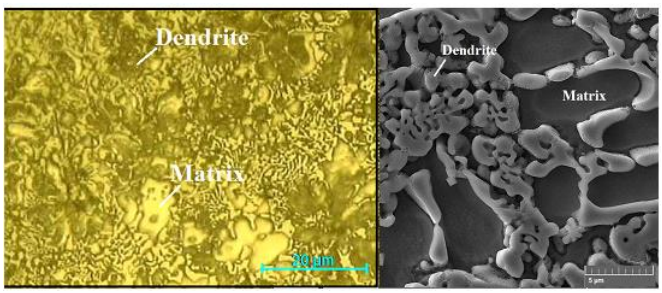

Figure 20. Microstructures of Zone 2 of C3 sample at greater magnifications

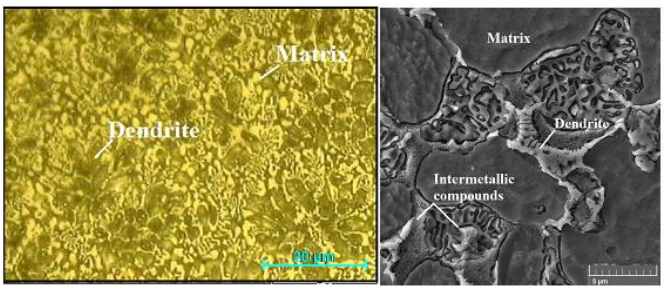

Figure 21. Microstructures of Zone 3 of C3 sample at greater magnifications

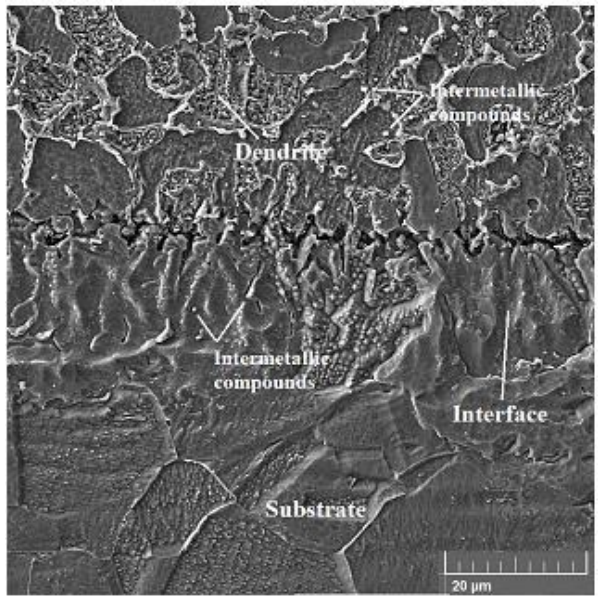

Figure 22. Microstructure of scanning electrons of the C3 interface

The main constituents of the C3 sample that appeared in the XRD examination (Figure 23) were similar to those of the C2 sample, except that the $Fe_{0.93}Ni_{0.058}$ compound did not clearly appear.

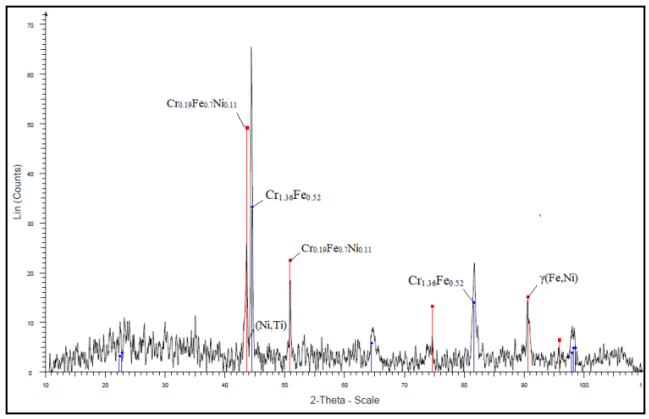

Figure 23. XRD graph of the surface of the C3 clad layer

Figure 24 demonstrates the microstructures at different depths along the centerline of the cross section of the C4 clad layer, and Figures 25-27 show these microstructures at higher magnifications. It is clearly observed that the size of the dendrites and their distribution in the microstructures along the centerline of the cross section of this clad layer are somewhat similar to what appeared in the C3 clad layer.

Table 8 exhibits that the average content of iron and chromium elements at the three test points of this sample, compared to the C3 sample, is notably higher (53.9 wt.% and 13.7 wt.% respectively) at the expense of average nickel and titanium element contents (20.2 wt.% and 12.2 wt.% respectively). This is due to the increased cladding current value to 140 A, which in turn leads to increased dilution with the substrate.

The contents of Fe and Cr elements in Zone 3, compared to those in Zones 1 and 2, are slightly higher at the expense of Ni and Ti contents, due to the proximity of this zone to the substrate, and thus more dilution occurs.

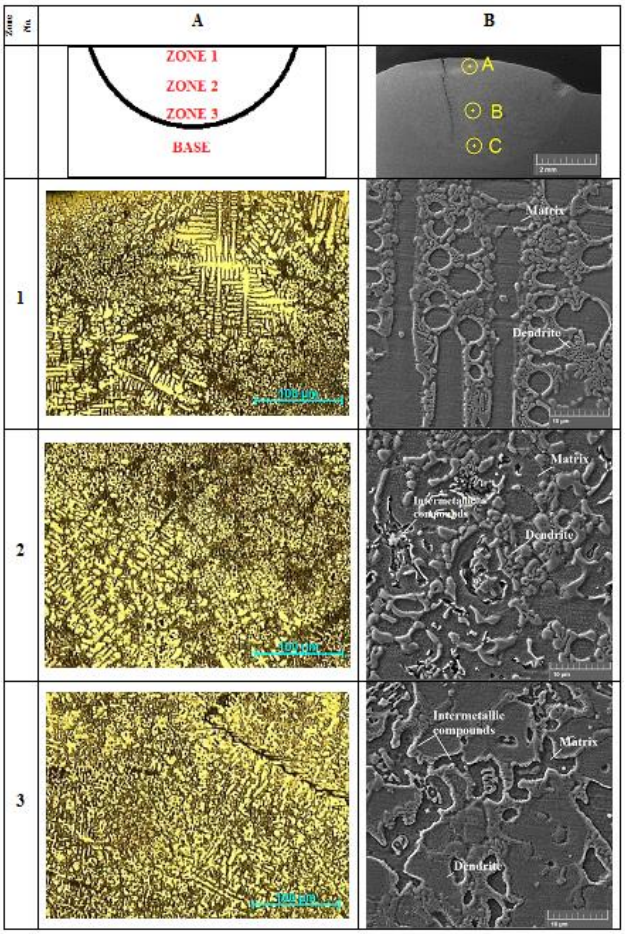

Figure 24. The C4 sample's microstructural map created using (A) OM and (B) SEM at different depths along the clad layer cross section's centerline

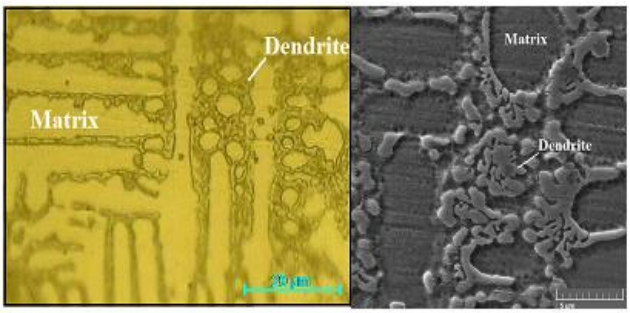

Figure 25. Microstructures of Zone 1 of C4 sample at greater magnifications

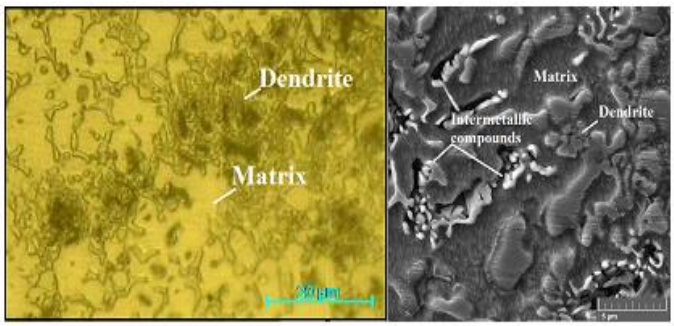

Figure 26. Microstructures of Zone 2 of C4 sample at greater magnifications

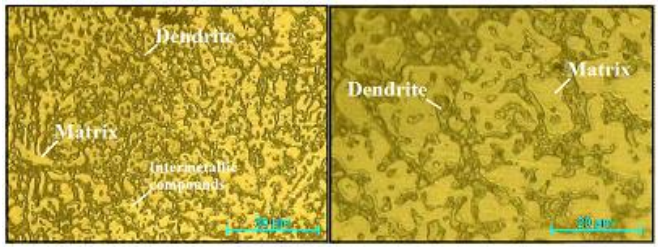

Figure 27. Optical microstructures of Zone 3 of C4 sample at increased magnification

Table 8. The C4 sample's elemental composition analyzed using EDS at different depths along the clad layer cross section's centerline

Element	Zone 1 [wt.%]	Zone 2 [wt.%]	Zone 3 [wt.%]
Ni	19.86	21.46	19.37
Ti	12.44	12.93	11.16
Cr	13.57	13.65	13.91
Fe	54.13	51.97	55.56

Figure 28 reveals that the main constituents of the C4 sample appeared in the XRD examination were somewhat similar to those of the previous clad layers.

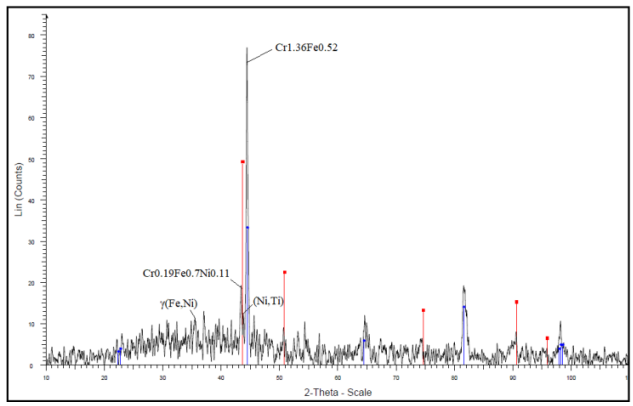

Figure 28. XRD graph of the surface of the C4 clad layer

Compared to the C4 sample, increasing the TIG cladding current value to 160 A at the same travel speed of 87 mm/min. in the C5 sample, resulting in a finer structure, as shown in Figure 29. Figures 30-32 show the microstructures at different depths along the centerline of the C5 cross section with higher magnifications. Figure 33 exhibits a reliable bonding with the substrate due to the relatively higher dilution with the substrate material as a result of the increased value of the cladding current.

The EDS analysis exhibits in Table 9 that the average content of iron, chromium, nickel, and titanium elements at the three test points of this sample (52.8 wt.%, 13.4 wt.%, 20.2 wt.% and 13.6 wt.% respectively) is close to that of the C4 sample.

The contents of Fe and Cr in Zone 3, compared to those in Zones 1 and 2, are also slightly higher at the expense of Ni and Ti contents, due to the proximity of this zone to the substrate, and thus more dilution occurs.

XRD examination of the C5 surface revealed in Figure 34 that the main constituents of this clad layer are NiTi solid solution and (Fe,Cr) and γ(Fe,Ni), in addition to $Cr_{0.19}Fe_{0.7}Ni_{0.11}$, $Cr_{1.36}Fe_{0.52}$ and $Fe_{0.93}Ni_{0.058}$ compounds.

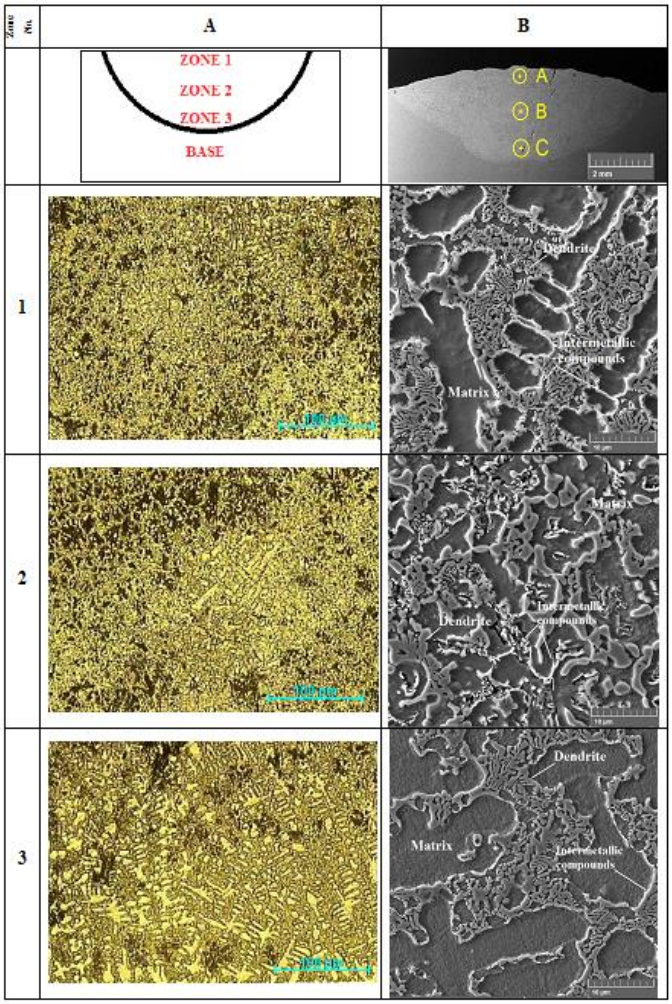

Figure 29. The C5 sample's microstructural map created using (A) OM and (B) SEM at different depths along the clad layer cross section's centerline

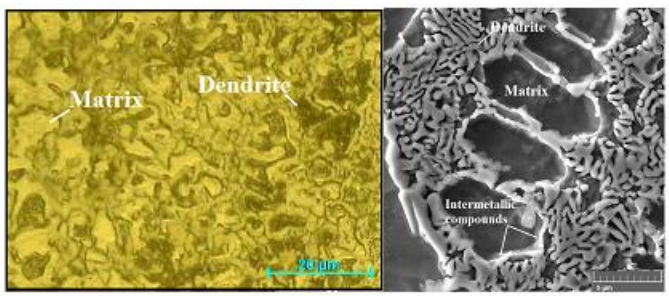

Figure 30. Microstructures of Zone 1 of C5 sample at greater magnifications

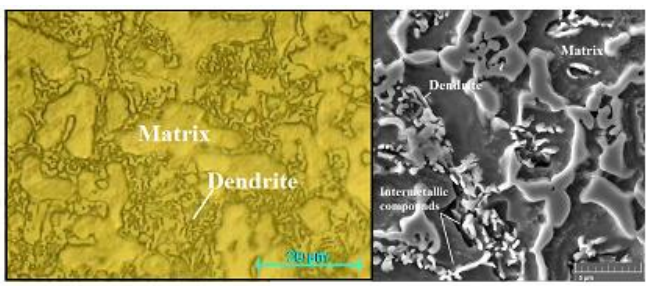

Figure 31. Microstructures of Zone 2 of C5 sample at greater magnifications

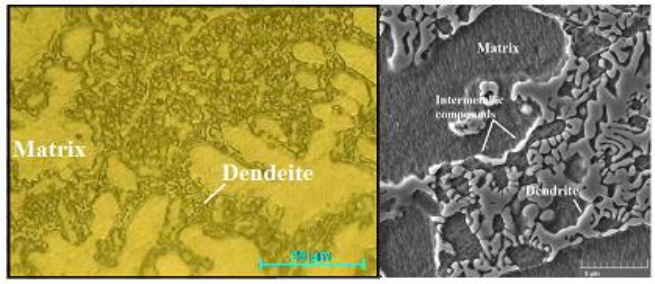

Figure 32. Microstructures of Zone 3 of C5 sample at greater magnifications

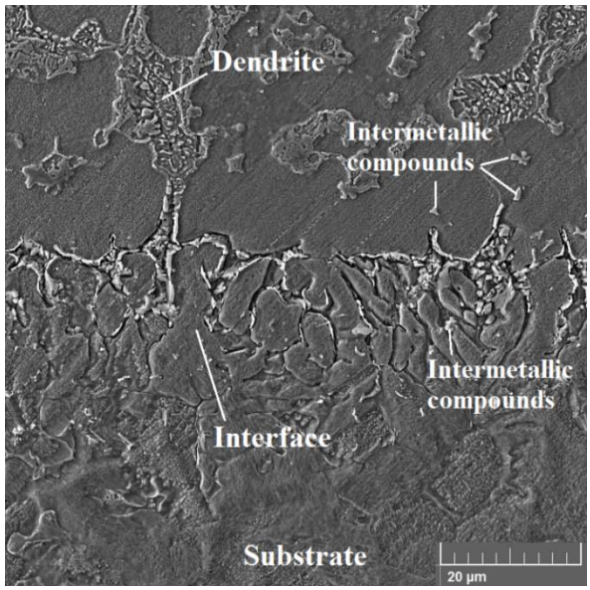

Figure 33. Scanning electron microstructure of the C5 interface

Table 9. The C5 sample's elemental composition analyzed using EDS at different depths along the clad layer cross section's centerline

Element	Zone 1 [wt.%]	Zone 2 [wt.%]	Zone 3 [wt.%]
Ni	20.75	19.94	19.90
Ti	15.28	13.46	12.13
Cr	12.32	13.76	14.02
Fe	51.66	52.83	53.94

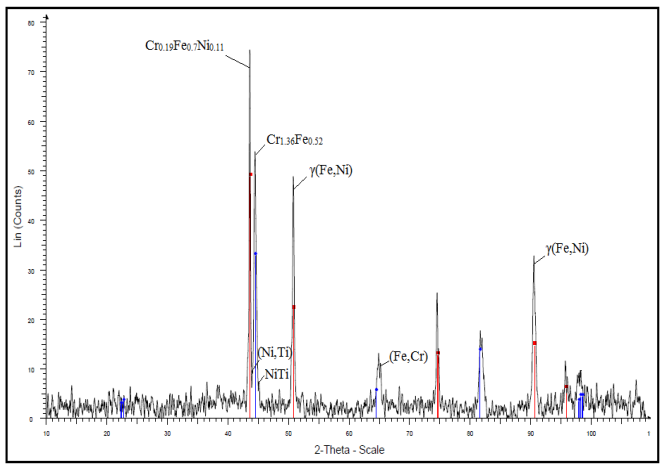

Figure 34. XRD graph of the surface of the C5 clad layer

4. CONCLUSIONS

This research investigated the impact of using various TIG cladding current values (80, 100, 120, 140 and 160 A) on microstructure of NiTi coating layer deposited on substrates made of austenitic stainless steel. The following conclusions can be drawn from the study's most significant findings:

1. Microstructures throughout the clad layers were mainly NiTi-based solid solution dendrites with minor phase precipitates (micrometers or less) distributed through the matrix.

2. The cladding current value, and hence heat energy input, had a significant influence on the grain size of the structure.

3. Increasing the cladding current value resulted in a significant increase in the dendritic content at the expense of the matrix in the microstructure of the clad layers

4. The increase in the cladding current value resulted in a significant increase in the proportion of intermetallic compounds at the clad layer-substrate interfaces.

5. Increasing the cladding current intensity resulted in a notable increase in the amount of chromium and iron elements diluted from the AISI 316 stainless steel substrate into the NiTi layer at the expense of nickel and titanium contents.

6. The diluted elements led to the formation of a B2 (NiTiFeCr) dendritic structure during solidification. Different phases and compounds, mainly NiTi solid solution, γ(Fe,Ni), $Cr_{0.19}Fe_{0.7}Ni_{0.11}$ and $Cr_{1.36}Fe_{0.52}$ formed the coating layers.

5. RECOMMENDATIONS

This study provides valuable insights for future cladding research. To further enhance this work, the following areas are recommended for exploration:

1. Corrosion examination for the clad layers can be conducted.

2. Laser cladding technology can be utilized with the clad layers.

3. Studying the influence of TIG cladding travel speed on the microstructure of the clad layers.

4. Investigating the mechanical characteristics of the clad layers.

REFERENCES

[1] Lo, K.H., Shek, C.H., Lai, J.K.L. (2009). Recent developments in stainless steels. Materials Science and Engineering: R: Reports, 65(4-6): 39-104. https://doi.org/10.1016/j.mser.2009.03.001

[2] Baddoo, N.R. (2008). Stainless steel in construction: Areview of research, applications, challenges andopportunities. Journal of Constructional steel Research, 64(11): 1199-1206. https://doi.org/10.1016/j.jcsr.2008.07.011

[3] Rossi, B. (2014). Discussion on the use of stainless steel in constructions in view of sustainability. Thin-Walled Structures, 83: 182-189. https://doi.org/10.1016/j.tws.2014.01.021

[4] Sheets, A.S.G.D. (2013). Atlas Steels Technical Handbook of Stainless Steels. Atlas Quality Management.

[5] Timings, R. (2008). Fabrication and Welding Engineering. London: Routledge. https://doi.org/10.4324/9780080886152

[6] Frenzel, J., George, E.P., Dlouhy, A., Somsen, C., Wagner, M.X., Eggeler, G. (2010). Influence of Ni on martensitic phase transformations in NiTi shape memory alloys. Acta Materialia, 58(9): 3444-3458. https://doi.org/10.1016/j.actamat.2010.02.019

[7] Duerig, T., Pelton, A., Stöckel, D.J.M.S. (1999). An overview of nitinol medical applications. Materials Science and Engineering: A, 273: 149-160. https://doi.org/10.1016/S0921-5093(99)00294-4

[8] Van Humbeeck, J. (1999). Non-medical applications of shape memory alloys. Materials Science and Engineering: A, 273: 134-148. https://doi.org/10.1016/S0921-5093(99)00293-2

[9] Wu, S.K., Lin, H.C., Yeh, C.H. (2000). A comparison of the cavitation erosion resistance of TiNi alloys, SUS304 stainless steel and Ni-based self-fluxing alloy. Wear, 244(1-2): 85-93. https://doi.org/10.1016/S0043-1648(00)00443-9

[10] Buehler, W.J., Wang, F.E. (1968). A summary of recent research on the nitinol alloys and their potential application in ocean engineering. Ocean Engineering, 1(1): 105-120. https://doi.org/10.1016/0029-8018(68)90019-X

[11] Richman, R.H., Rao, A.S., Hodgson, D.E. (1992). Cavitation erosion of two NiTi alloys. Wear, 157(2): 401-407. https://doi.org/10.1016/0043-1648(92)90076-K

[12] Cheng, F.T., Shi, P., Man, H.C. (2003). Cavitation erosion resistance of heat-treated NiTi. Materials Science and Engineering: A, 339(1-2): 312-317. https://doi.org/10.1016/S0921-5093(02)00162-4

[13] Li, D.Y. (2000). Exploration of TiNi shape memory alloy for potential application in a new area: Tribological engineering. Smart Materials and Structures, 9(5): 717. https://doi.org/10.1088/0964-1726/9/5/317

[14] Man, H.C., Zhang, S., Cheng, F.T., Guo, X. (2006). In situ formation of a TiN/Ti metal matrix composite gradient coating on NiTi by laser cladding and nitriding. Surface and Coatings Technology, 200(16-17): 4961-4966. https://doi.org/10.1016/j.surfcoat.2005.05.017

[15] Cheng, F.T., Lo, K.H., Man, H.C. (2004). A preliminary study of laser cladding of AISI 316 stainless steel using preplaced NiTi wire. Materials Science and Engineering: A, 380(1-2): 20-29. https://doi.org/10.1016/j.msea.2004.01.056

[16] Chiu, K.Y., Cheng, F.T., Man, H.C. (2005). Laser cladding of austenitic stainless steel using NiTi strips for resisting cavitation erosion. Materials Science and Engineering: A, 402(1-2): 126-134. https://doi.org/10.1016/j.msea.2005.04.013

[17] Zarghami, K., Khademzadeh, S., Parvin, N., Azarmehr, Y. (2021). The role of scanning velocity on laser cladding of NiTi alloy onto stainless steel 316L substrate. The International Journal of Advanced Manufacturing Technology, 117(7): 2029-2039. https://doi.org/10.1007/s00170-021-07112-4

[18] Kumar, P., Sinha, A.N., Saravanan, A., Murugan, M., Hirwani, C.K. (2021). Study of microstructure and mechanical properties of NiTi wire cladding on super austenitic stainless steel 904L by TIG cladding process. Sādhanā, 46: 1-16. https://doi.org/10.1007/s12046-021-01602-7

[19] Singh, J., Thakur, L., Angra, S. (2019). Effect of argon

flow rate and standoff distance on the microstructure and wear behaviour of WC-CoCr TIG cladding. Journal of Physics: Conference Series, 1240(1): 012162. https://doi.org/10.1088/1742-6596/1240/1/012162

[20] Kilic, M., Imak, A., Kirik, I. (2021). Surface modification of AISI 304 stainless steel with NiBSi-SiC composite by TIG method. Journal of Materials Engineering and Performance, 30(2): 1411-1419. https://doi.org/10.1007/s11665-020-05378-5

[21] Cheng, F.T., Lo, K.A., Man, H.C. (2003). NiTi cladding on stainless steel by TIG surfacing process: Part I. Cavitation erosion behavior. Surface and Coatings Technology, 172(2-3), 308-315. https://doi.org/10.1016/S0257-8972(03)00345-1

[22] Guide, S.D. (2013). Structural Stainless Steel. American Institute of Steel Construction: Chicago, IL, USA.

[23] Jilabi, A.S.J., Oleiwi, A.A. (2024). Influence of WC content on microstructure of WC-Ni coatings on AISI 18-2Mn austenitic stainless steel using TIG cladding. Annales de Chimie - Science des Matériaux, 48(4): 539-549. https://doi.org/10.18280/acsm.480411

[24] Padilha, A.F., Rios, P.R. (2002). Decomposition of Austenite in Austenitic Stainless Steels. ISIJ International, 42(4): 325-337. https://doi.org/10.2355/isijinternational.42.325

[25] Kliauga, A., Correa, L.M., Braga, D.P., Rovere, C.A.D., Cintho, O.M., Magalhães, D. (2024). Comprehensive Modeling of the Twip Effect Kinetics of 316 Lv Austenitic Stainless Steel: Decoupling Dislocation Glide, Back Stress and Mechanical Twinning Contributions. SSRN. https://papers.ssrn.com/sol3/papers.cfm?abstract_id=4758822.

[26] Byun, T., Hashimoto, N. (2008). Strain hardening during mechanical twinning and dislocation channeling in irradiated 316 stainless steels. In Effects of Radiation on Materials: 23rd International Symposium. ASTM International. https://doi.org/10.1520/STP46568S

[27] Mehrer, H. (2007). Diffusion in Solids: Fundamentals, Methods, Materials, Diffusion-Controlled Processes. Springer Science & Business Media.

[28] Ozel, S., Kurt, B., Somunkiran, I., Orhan, N. (2008). Microstructural characteristic of NiTi coating on stainless steel by plasma transferred arc process. Surface and Coatings Technology, 202(15): 3633-3637. https://doi.org/10.1016/j.surfcoat.2008.01.006

[29] Zhang, C.H., Li, S., Qi, L., Ren, Y.H., Zhang, S., Wang, M.C. (2012). Fabrication of NiTi alloy coating on 2Cr13 stainless steel by lasr cladding. Advanced Materials Research, 418: 242-245. https://doi.org/10.4028/www.scientific.net/AMR.418-420.242

[30] Islak, S., Buytoz, S., Karagöz, M. (2012). Microstructural development on AISI 1060 steel by FeW/B_4C composite coating produced by using tungsten inert gas (TIG) process. Indian Journal of Engineering and Materials Sciences, 19(4): 253-259.

[31] Shi, Z.P., Wang, Z.B., Wang, J.Q., Qiao, Y.X., Chen, H.N., Xiong, T.Y., Zheng, Y.G. (2020). Effect of Ni interlayer on cavitation erosion resistance of NiTi cladding by tungsten inert gas (TIG) surfacing process. Acta Metallurgica Sinica (English Letters), 33: 415-424. https://doi.org/10.1007/s40195-019-00947-7

[32] Mridha, S., Baker, T.N. (2015). Overlapping tracks processed by TIG melting TiC preplaced powder on low alloy steel surfaces. Materials Science and Technology, 31(3): 337-343. https://doi.org/10.1179/1743284714Y.0000000530